










N-Heterocyclic carbene-based C-centered Au(I)-Ag(I) clusters with intense phosphorescence and organelle-selective translocation in cells

Zhen Lei ^{1,5}, Mizuki Endo ^{1,5}, Hitoshi Ube ¹, Takafumi Shiraogawa², Pei Zhao ², Koichi Nagata ^{1,4}, Xiao-Li Pei¹, Tomoya Eguchi³, Toshiaki Kamachi ³, Masahiro Ehara ²✉, Takeaki Ozawa ¹✉ & Mitsuhiro Shionoya ¹✉

Photoluminescent gold clusters are functionally variable chemical modules by ligand design. Chemical modification of protective ligands and introduction of different metals into the gold clusters lead to discover unique chemical and physical properties based on their significantly perturbed electronic structures. Here we report the synthesis of carbon-centered Au(I)-Ag(I) clusters with high phosphorescence quantum yields using *N*-heterocyclic carbene ligands. Specifically, a heterometallic cluster [(C)(Au^I-L)₆Ag^I]₂⁴⁺, where L denotes benzimidazolylidene-based carbene ligands featuring *N*-pyridyl substituents, shows a significantly high phosphorescence quantum yield ($\Phi = 0.88$). Theoretical calculations suggest that the carbene ligands accelerate the radiative decay by affecting the spin-orbit coupling, and the benzimidazolylidene ligands further suppress the non-radiative pathway. Furthermore, these clusters with carbene ligands are taken up into cells, emit phosphorescence and translocate to a particular organelle. Such well-defined, highly phosphorescent C-centered Au(I)-Ag(I) clusters will enable ligand-specific, organelle-selective phosphorescence imaging and dynamic analysis of molecular distribution and translocation pathways in cells.

¹Department of Chemistry, Graduate School of Science, The University of Tokyo, 7-3-1 Hongo, Bunkyo-ku, Tokyo 113-0033, Japan. ²Research Center for Computational Science, Institute for Molecular Science and SOKENDAI, Myodaiji, Okazaki, Aichi 444-8585, Japan. ³Department of Life Science and Technology, Tokyo Institute of Technology, 2-12-1-M6-7 Ookayama, Meguro-ku, Tokyo 152-8550, Japan. ⁴Present address: Department of Chemistry, Graduate School of Science, Tohoku University, Aoba-ku, Sendai, Miyagi 980-8578, Japan. ⁵These authors contributed equally: Zhen Lei, Mizuki Endo. ✉email: ehara@ims.ac.jp; ozawa@chem.s.u-tokyo.ac.jp; shionoya@chem.s.u-tokyo.ac.jp

Sub-nanoscale gold clusters with atomic precision are promising miniature nanoscale materials. Gold clusters often exhibit photoluminescence properties such as phosphorescence, in addition to the unique molecular structures and aurophilicity^{1,2}. To date, several excellent protocols have been developed to improve the photoluminescence performance of gold clusters. Examples include alloying by metal kernels, supramolecular networking by self-assembly of clusters, surface hardening by additives, chemical modification by capping ligands with electron-donating/withdrawing groups, and so on^{3–10}. The structure, electronic state, and reactivity of the gold cluster moiety can be greatly affected by the protective ligands and different metals that additionally bind to the gold atoms.

The octahedral hexagold(I) cluster with a hyper-coordinated carbon center (CAu₆^I), first developed by Schmidbaur et al. using phosphine ligands, is one of the most classical models of Au^I clusters^{11,12}. These clusters emit bright yellowish-green light in the solid-state, but not in solution. Wang et al. reported a heteronuclear metal cluster capable of emitting light even in solution by the pyridyl-phosphine bidentate ligand^{13,14}. This method has made it possible to construct a series of heterometallic Au^I clusters that exhibit strong red phosphorescence in solution^{15,16}. This luminescence is thought to be due to the formation of a solid sphere in which the surface of the cluster is completely protected¹⁷. It has also been reported that such cluster complexes are a promising group of compounds that emit light at specific locations in the cell¹⁸.

More recently, *N*-heterocyclic carbene (NHC) ligands have been developed as one of the most promising organic ligands for Au⁰ clusters with high designability^{19–22}. Carbene ligands have strong electron-donating properties and are known to enhance the stability of metal surfaces, metal nanoparticles, and metal nanorods^{23–25}. Therefore, NHC ligands have been used in the synthesis of Au⁰ clusters^{26–30}, and their interfacial structure, stability, and catalytic activity have been elucidated. In this context, we successfully applied the NHC ligand to the CAu^I₆ cluster in 2018^{31–33}. We found that when an imidazolylidene carbene ligand was attached to each gold atom of the C-centered CAu^I₆ cluster, the phosphorescence emission was red-shifted in the solid-state compared to clusters protected by phosphine ligands³¹. On the other hand, when a benzimidazolylidene ligand with one benzene ring fused to the imidazole ring was used, the phosphorescence emission showed a large blue shift of about 60 nm^{32,33}. These two examples indicate that such a simple chemical modification can significantly change the photochemical properties of the clusters. Phosphorescent metal cluster complexes have the potential to precisely control the structure and electronic state of the metal cluster part by ligand design, and are expected to contribute not only to the creation of structure-specific photochemical functions but also to live-cell imaging and elucidation of intracellular molecular behaviors.

In this study, we design and synthesize bidentate ligands consisting of an NHC ligand linked to a pyridyl ligand, and clarify the detailed structure and photochemical properties of heteronuclear clusters of Au^I and Ag^I, which exhibit very high phosphorescence quantum yields even in solution. Furthermore, the strong phosphorescence emission of these clusters is used to elucidate the cellular uptake and organelle-selective translocation pathways of the cluster complexes (Fig. 1). Interestingly, the NHC ligand-protected heterometallic clusters are translocated to a specific intracellular organelle in a ligand-specific manner. This is in sharp contrast to phosphine-protected clusters with the same metal core structure, which are non-selectively dispersed in the cytosol. Thus, the control of intracellular translocation of C-centered Au^I clusters is achieved by a slight modification of organic ligands. These results not only show that NHC ligands

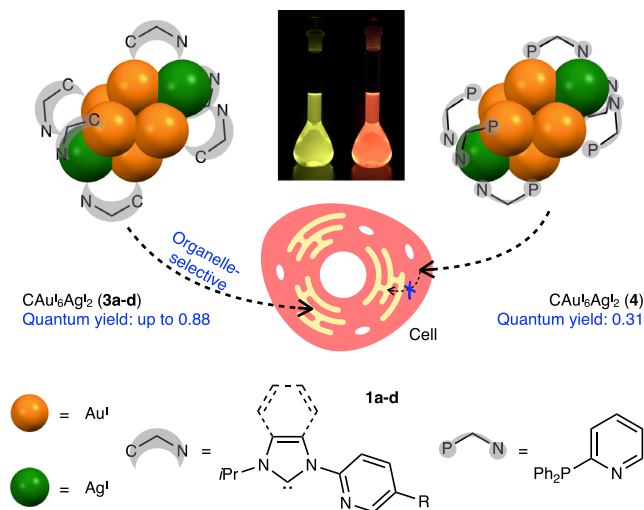


Fig. 1 Schematic diagram of this study. Carbon(C)-centered Au^I-Ag^I clusters with *N*-heterocyclic carbene (NHC) ligands with intense phosphorescence and their ligand-specific, organelle-selective translocation in cells.

can improve the phosphorescence emission efficiency of C-centered Au^I clusters, but also guide the development of functions for metal cluster-based functional molecules in chemical synthesis approaches.

Results

Synthesis and characterization. To further polynucleate the Au^I cluster with different metals, a nitrogen donor was introduced into the wing-tip portion of each NHC ligand (*N*-isopropyl-*N'*-2-(5-methylpyridyl)benzimidazolylidene (**1a**), *N*-isopropyl-*N'*-2-pyridylbenzimidazolylidene (**1b**), *N*-isopropyl-*N'*-2-(5-methylpyridyl)imidazolylidene (**1c**), *N*-isopropyl-*N'*-2-pyridylimidazolylidene (**1d**); Supplementary Figs. 1–4). Specifically, CAu^I₆ complexes [(C)(Au^I-L)₆](BF₄)₂ (**2a–d**, L = **1a–d**) in which only the carbene ligand is coordinated to Au^I, were synthesized from unsymmetrical bidentate ligands **1a–d**. The isolation yields of **2a–d** were 8–52% based on the amount of Au^I used according to previously reported literatures^{11–18}, and their molecular structures in the solid-state were determined by single-crystal X-ray diffraction (ScXRD) (Fig. 2, Supplementary Figs. 5, 6, and Supplementary Table 8). It was found by NMR spectroscopy (Supplementary Figs. 8–27) and mass spectrometry (Supplementary Fig. 28) that the solid-state structure was maintained in solution.

The heterometallic CAu^I₆Ag^I₂ clusters, [(C)(Au^I-L)₆Ag^I₂](BF₄)₄ (**3a–d**, L = **1a–d**) were synthesized from CAu^I₆ clusters **2a–d** with pyridyl pendants-introduced ligands **1a–d**. The processes of complexation of CAu^I₆ clusters **2a–d** with AgBF₄ were investigated by UV-vis absorption, phosphorescence spectroscopy, mass spectrometry, and NMR spectroscopy (Supplementary Figs. 34–46). CAu^I₆Ag^I₂ clusters, **3a–d**, were isolated as single crystals by layering dry Et₂O on a solution of each reaction mixture in CH₂Cl₂/CH₃OH. As shown in Fig. 3a, the molecular structures of CAu^I₆Ag^I₂ clusters, [(C)(Au^I-L)₆Ag^I₂](BF₄)₄ (**3a–d**, L = **1a–d**), were determined by ScXRD, and all clusters were found to have a bicapped octahedral core. The two Ag^I ions in each cluster are located on two opposite sides of the octahedron, each anchored by three pyridyl groups and interacting with three neighboring Au^I atoms. These CAu^I₆Ag^I₂ clusters **3a–d** showed strong intramolecular C–H⋯Au interactions^{34–36}, with the shortest H–Au distances being 2.690, 2.818, 2.765, and 2.730 Å, respectively (Supplementary Fig. 47). The structures are similar to

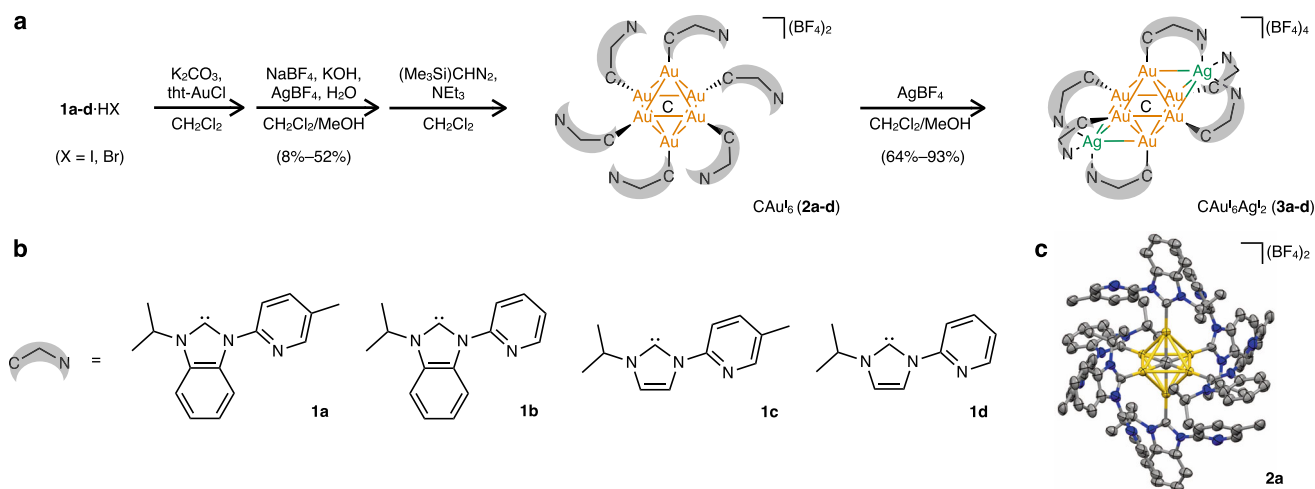


Fig. 2 Heteronuclear CAu_6Ag_2 clusters **3a–d** were used in this study. **a** Synthetic route for CAu_6Ag_2 clusters **3a–d**. **b** Chemical structures of ligands **1a–d**. **c** Molecular structure of $[(\text{C})(\text{Au}^{\text{I}}\text{-1a})_6](\text{BF}_4)_2$ (**2a**, 25% probability) with the anions BF_4^- simplified.

those of the previously reported $[(\text{C})(\text{Au}^{\text{I}}\text{-dppy})_6\text{Ag}_2](\text{BF}_4)_4$ (**4**, dppy = 2-pyridyldiphenylphosphine)¹⁴, but differ in the following two points. First, because the C – Au^{I} bond distances in **3a–d** with NHC ligands are shorter than those of the P – Au^{I} bonds in **4** with phosphine ligands, and also because the $\text{Au}^{\text{I}}\text{-Ag}^{\text{I}}$ distances are shorter in **3a–d**, the overall structures of the CAu_6Ag_2 parts of **3a–d** are significantly smaller than that of **4** (Fig. 3b). The $\text{Au}^{\text{I}}\text{-Ag}^{\text{I}}$ distances in **3a–d** are in a very similar range (Supplementary Table 13). Second, there are no intramolecular C – H...Au interactions in **4**.

Upon photoexcitation, **3a–d** showed strong yellow luminescence in the solid-state with $\lambda_{\text{em}}^{\text{max}}$ lying in the range from 559 to 578 nm, which significantly red-shifted as compared to **2a–d** (from 482 to 490 nm), and is similar to **4** (553 nm, Fig. 3c and Supplementary Figs. 29 and 48). The two Ag^{I} atoms do not simply bind to the CAu_6 core but may change the electronic structure of the whole clusters^{13–17}.

The CAu_6Ag_2 clusters **3a–d** were further characterized by solution-phase NMR spectroscopy (Supplementary Figs. 49–64). Two interesting features were observed in the ^1H NMR spectra. First, in the ^1H NMR spectra of **3a–d**, the septet signals of the secondary hydrogen atoms of the isopropyl groups were shifted to the high field by about 0.5 ppm compared to **2a–d**, which is a change similar to that observed when AgBF_4 was added to **2a–d** (Supplementary Figs. 42–45). This result confirmed the existence of C – H...Au interactions in **3a–d** even in solution³⁶. The second feature is that split signals of methyl of isopropyl groups were observed in the both ^1H and ^{13}C NMR spectra of **3a–d**. For example, the methyl groups of **2b** showed only one set of signals in the ^1H (1.49 ppm) and ^{13}C NMR (21.9 ppm) spectra, whereas two sets of signals were observed in the ^1H NMR (1.44 and 1.33 ppm) and ^{13}C NMR (22.6 and 22.1 ppm) spectra for **3b**. It was inferred from the molecular structures of **3a–d** that this signal change was caused by the helical arrangement of the ligands in the bicapped octahedral CAu_6Ag_2 and the two opposing CAu_3Ag_1 moieties showing different helical directions^{14,15}. Heterometallic species, $[(\text{C})(\text{Au}^{\text{I}}\text{-L})_4\text{Au}^{\text{I}}\text{Ag}^{\text{I}}](\text{BF}_4)^+$ and $[(\text{C})(\text{Au}^{\text{I}}\text{-L})_6\text{Ag}^{\text{I}}](\text{BF}_4)_2^+$ (L = **1a–d**), were also observed in the MS spectra (Supplementary Fig. 65). These results strongly suggest that all of **3a–d** maintain the bicapped octahedral structures even in solution.

Solutions of CAu_6Ag_2 clusters **3a–d** in CH_2Cl_2 or $\text{CH}_2\text{Cl}_2/\text{CH}_3\text{OH}$ showed multiple optical absorption bands in the range of 300–450 nm (Fig. 3d). These optical absorption modes were

consistent with those observed when AgBF_4 was added to the solutions of **2a–d**. Their molar absorbance coefficients of **3a** and **3b**, protected with benzimidazolylidene ligands, were significantly higher than those of **3c** and **3d**, protected with imidazolylidene ligands.

Importantly, the use of the bidentate NHC ligands and the coordination of Ag^{I} ions have a synergistic effect, and the heterogeneous metal clusters emit very strong phosphorescence in solution (Fig. 3e and Supplementary Fig. 66). In comparison, the metal clusters **3a–d** with NHC ligands emit yellow light in solution, whereas **4** with phosphine ligands emit red phosphorescence, with a difference in wavelength of about 90 nm. The phosphorescence quantum yields of **3a** and **3b** were determined to be 0.88 and 0.86 in CH_2Cl_2 ($\lambda_{\text{em}}^{\text{max}} = 562$ nm), respectively, the highest values among the reported Au^{I} clusters (Fig. 3g). In contrast, single crystals of **3c** and **3d** with imidazolylidene ligands showed similar yellow luminescence, but the phosphorescence quantum yields in CH_2Cl_2 and $\text{CH}_2\text{Cl}_2/\text{CH}_3\text{OH}$ were remarkably low, 0.14 and 0.01, respectively. In addition, the phosphorescence lifetimes of **3a** and **3b** protected with benzimidazolylidene ligands were 1.85 and 1.66 μs , respectively, which were significantly longer than those of **3c** and **3d** protected with imidazolylidene ligands, 0.32 and 0.16 μs , respectively (Fig. 3f). The radiative (k_r) and non-radiative rate constants (k_{nr}) shown in Fig. 3g indicate that clusters with NHC ligands have significantly higher radiative emission rates than clusters with phosphine ligands. Furthermore, the benzimidazolylidene ligand could dramatically improve the quantum yield and microsecond-level lifetime of the phosphorescence of the CAu_6Ag_2 clusters, **3a** and **3b**, by significantly suppressing the non-radiative relaxation pathways.

Theoretical calculations of CAu_6Ag_2 clusters. In order to mechanistically clarify how the photochemical properties change depending on the type of carbene ligands, the absorption and phosphorescence properties of **3b** with benzimidazolylidene ligands and **3d** with imidazolylidene ligands were theoretically calculated and comparatively analyzed (Fig. 4). As a result, the calculated absorption spectra agreed well with the experimental observations in the calculated energy range. The trend of the energy difference was reproduced; the first peaks for **3b** and **3d** were calculated to be 387 and 388 nm, respectively. The order of the molar absorbance coefficients (**3b** > **3d**) was also well

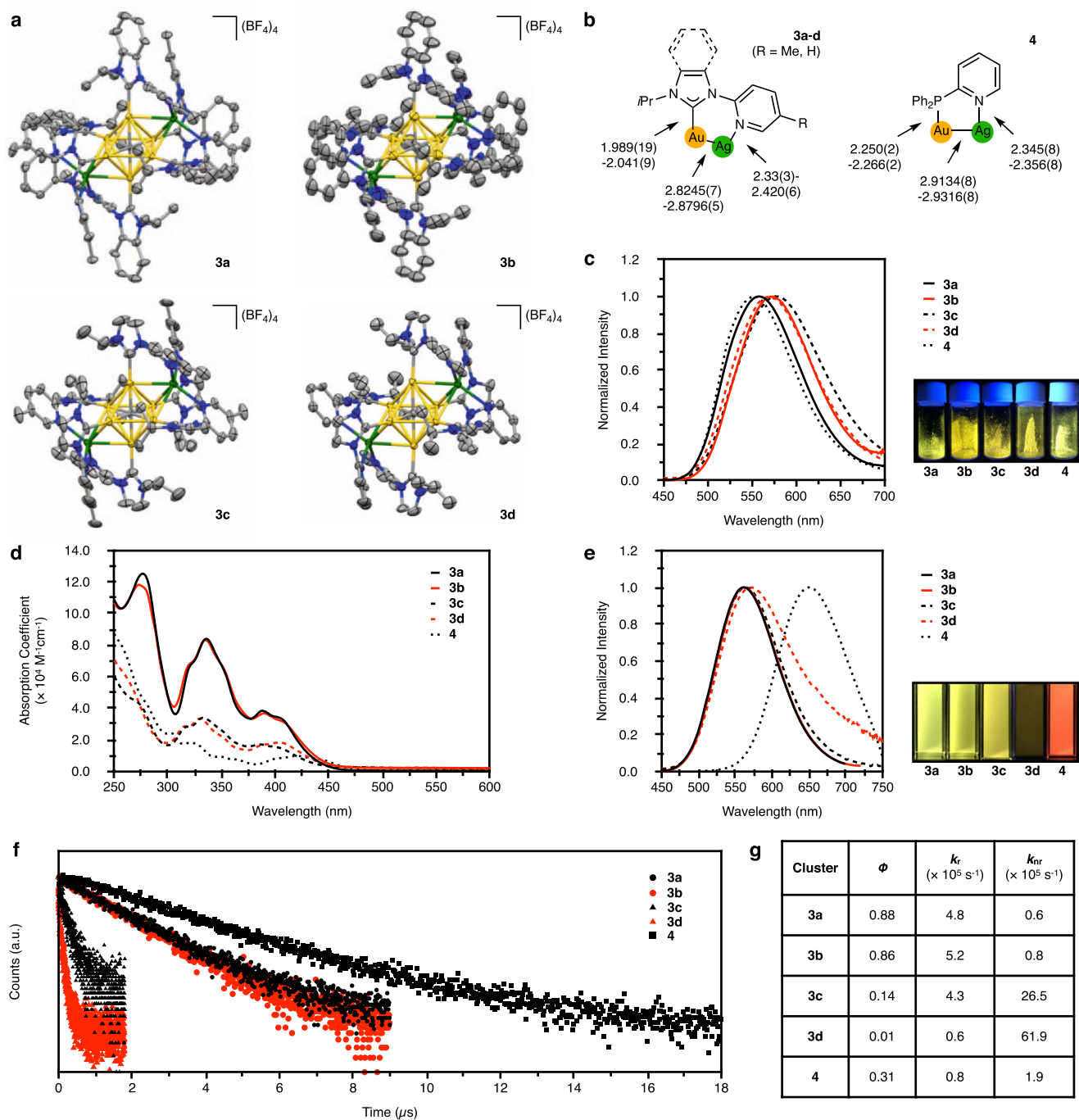


Fig. 3 Molecular structures and photochemical properties of $\text{CAu}_6\text{Ag}_{12}$ clusters **3a-d** and **4**. **a** Molecular structures of **3a-d** (50% probability for **3a**, **3c**, and **3d**; 25% probability for **3b**), with the anions BF_4^- simplified. **b** Comparison of the key structure parameters of **3a-d** and **4**. **c** Emission spectra of **3a-d** and **4** in the solid-state, with $\lambda_{\text{em}}^{\text{max}}$ being 559, 573, 578, 570, and 553 nm, respectively, and corresponding photos at room temperature. **d** UV-vis absorption spectra of **3a** ($\epsilon_{336} = 8.4 \times 10^4 \text{ M}^{-1} \text{ cm}^{-1}$), **3b** ($\epsilon_{336} = 8.3 \times 10^4 \text{ M}^{-1} \text{ cm}^{-1}$), **3c** ($\epsilon_{333} = 3.4 \times 10^4 \text{ M}^{-1} \text{ cm}^{-1}$), **3d** ($\epsilon_{330} = 3.3 \times 10^4 \text{ M}^{-1} \text{ cm}^{-1}$), and **4** ($\epsilon_{321} = 1.8 \times 10^4 \text{ M}^{-1} \text{ cm}^{-1}$) in CH_2Cl_2 (293 K). **e** Emission spectra of **3a-d** and **4** in CH_2Cl_2 at 293 K, with $\lambda_{\text{em}}^{\text{max}}$ of 562, 562, 564, 571, and 650 nm, respectively, and the corresponding photos taken at room temperature. **f** Emission decay of **3a-d** and **4** in CH_2Cl_2 at room temperature, with τ of 1.85, 1.66, 0.32, 0.16, and 3.74 μs , respectively. **g** Quantum yields, radiative rate constants (k_r) and non-radiative rate constants (k_{nr}) of **3a-d** and **4** in CH_2Cl_2 at room temperature. Note that a mixed solvent $\text{CH}_2\text{Cl}_2/\text{CH}_3\text{OH}$ (9:1, v:v) was used for **3d**⁴².

reproduced. The distributions of SOMO and SOMO - 1, which characterize phosphorescence, are similar to those of LUMO and HOMO, respectively (Fig. 4c, d). The imidazolylidene and benzimidazolylidene ligand moieties are involved in the SOMO - 1 orbitals. The calculated phosphorescence energies of **3b** and **3d** are 2.09 and 2.08 eV (592 and 596 nm, respectively), which are in

close agreement with the experimental values of 2.21 and 2.17 eV, respectively, within error³⁷ (Supplementary Table 21).

It is worth noting that the molecular structure of the clusters in the singlet state is very different from that in the triplet state^{8,9,38,39} (Supplementary Fig. 71 and Supplementary Table 23). For example, the $\text{Au}^{\text{I}}-\text{Au}^{\text{I}}$ distances of **3b** in the

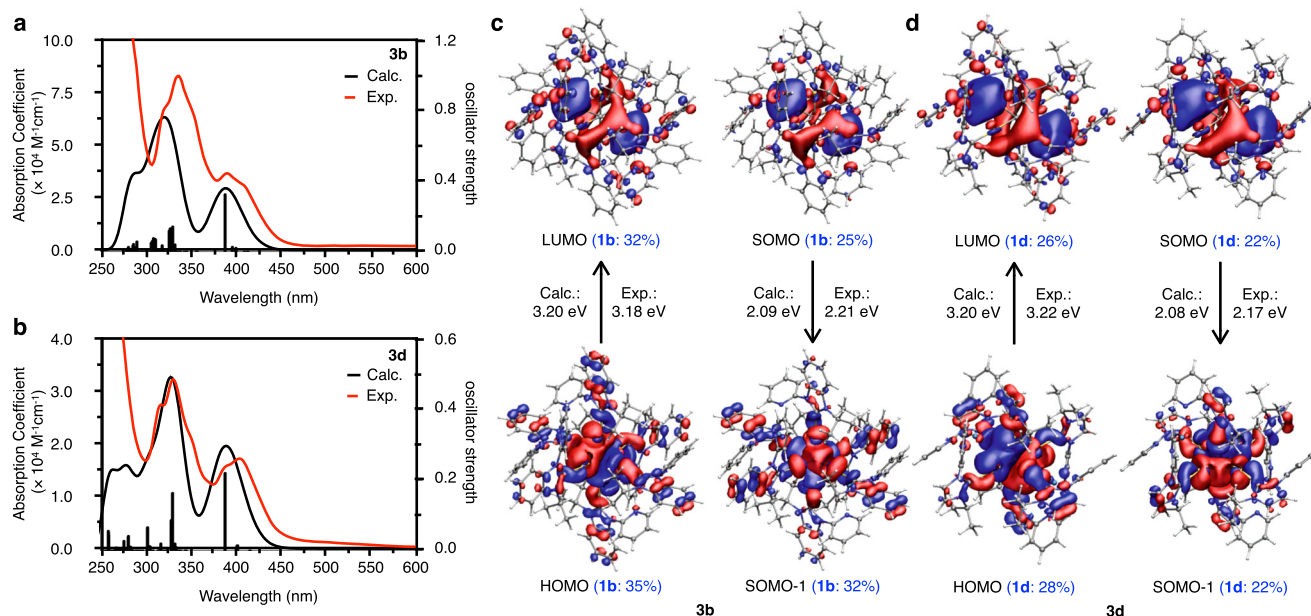


Fig. 4 TD-DFT calculations for $\text{CAu}^{\text{I}}_6\text{Ag}^{\text{I}}_2$ clusters **3b** and **3d**. **a, b** Calculated and experimental absorption spectra of **3b** (calc. $\epsilon_{388} = 3.0 \times 10^4 \text{ M}^{-1} \text{ cm}^{-1}$, exp. $\epsilon_{390} = 3.7 \times 10^4 \text{ M}^{-1} \text{ cm}^{-1}$) and **3d** (calc. $\epsilon_{389} = 2.0 \times 10^4 \text{ M}^{-1} \text{ cm}^{-1}$, exp. $\epsilon_{385} = 1.6 \times 10^4 \text{ M}^{-1} \text{ cm}^{-1}$). The excitation energies, oscillator strengths, and transition characters for the absorption spectra are summarized in Supplementary Tables 18, 19, and the associated molecular orbitals (MOs) are shown in Supplementary Figs. 68, 69. The lowest peaks observed around 400 nm for **3b** and **3d** were considered to be transitions between MOs consisting mainly of Au^{I} , Ag^{I} and the central carbon. The strong absorption peaks around 330 nm for **3b** and **3d** are due to the MLCT transition from Au^{I} to ligands³⁷. The absorption in the high-energy region (<300 nm) is mainly due to the $\pi\pi^*$ transition of the ligands. **c, d** Calculated MOs (lowest unoccupied molecular orbital, LUMO; highest occupied molecular orbital, HOMO; singly occupied molecular orbital, SOMO, in the triplet state), comparisons of calculated and experimental excitation energies, and analysis of orbital composition by Mulliken partition of ligands in **3b** and **3d**.

singlet state were found to be in the range of 3.090–3.203 Å, while in the triplet state they were found to be in the range of 2.931–3.443 Å. Therefore, we quantitatively analyzed the orbital compositions to evaluate the ligand effects. Mulliken partition analysis confirmed that even though the core of $\text{CAu}^{\text{I}}_6\text{Ag}^{\text{I}}_2$ is mainly involved in the MOs, the ligands make significant contributions (Supplementary Tables 24–26). Unlike the phosphine ligand, the carbene ligand reduced the involvement of the ligand in the frontier orbitals and suppressed the involvement of the ligand in the charge transfer processes (see Supplementary Information for the details).

We then directly investigated the phosphorescence lifetimes and the radiative rate constants of **3b** and **3d** using the ZORA method with spin–orbit interaction in a perturbative way⁴⁰ implemented in the ADF program package⁴¹. The results are compared to the experimental values, which approximate the calculated k_r as $k_r = 1/\tau$ (Supplementary Table 27). The phosphorescence is attributed to the three lowest, nearly degenerate spin–orbit states, which are about 0.1 eV lower than other states, with T_1 being the dominant contribution. Although the order of the absolute values of τ differs from the experimental values, the trend of k_r (**3b** > **3d**) agrees with each other. Importantly, the k_r values of imidazolylidene- and benzimidazolylidene-protected clusters were almost quantitatively reproduced in the calculations. Note that the low k_r of **3d** with imidazolylidene ligands is due to the solvent effect of CH_3OH ⁴². In addition, we analyzed the wavefunction and spin–orbit coupling of the low-lying spin–orbit states (Supplementary Tables 27 and 28). These states are described mainly by the T_1 , T_2 , and T_3 components, with small contributions from the S_1 and S_3 components. It can be seen that the NHC ligand significantly changed the main component of each state and the coupling of the spin–orbit states. This is thought to be the origin of the different k_r values of these compounds.

Finally, in order to evaluate k_{nr} , the minimum energy crossing point (MECP) between S_0 and T_1 states was calculated using the Harvey method^{43,44}. The results showed that the core of $\text{CAu}^{\text{I}}_6\text{Ag}^{\text{I}}_2$ is significantly deformed at the MECP. For example, the shape of $\text{CAu}^{\text{I}}_6\text{Ag}^{\text{I}}_2$ of **3d** is significantly changed compared to the shape of the T_1 state (Supplementary Fig. 72). The energy barrier from the minimum of T_1 state to MECP were calculated as 11.6 and 10.8 kcal/mol for **3b** and **3d**, respectively, which qualitatively agrees with the k_{nr} of these complexes (Supplementary Table 29). However, the energy difference of the MECP for **3b** and **3d** is small, so there may be another cause. Overall, although NHC ligands are less involved in the electronic structure of the clusters than phosphine ligands, they can accelerate radiative decay by enhancing the spin–orbit coupling of the low-lying spin–orbit states. On the other hand, when the benzimidazolylidene ligand was used, non-radiative decays did not occur preferentially, resulting in **3a** and **3b** having very high quantum yields.

Ligand-specific translocation in cells. Luminescent metal complexes have been used as promising bioimaging reagents for the past two decades^{45–47}. Li and Wang et al. have reported on the nucleolus-selective labeling behavior of phosphine-protected $\text{CAu}^{\text{I}}_6\text{Ag}^{\text{I}}_2$ cluster **4**¹⁸. Since carbene-protected $\text{CAu}^{\text{I}}_6\text{Ag}^{\text{I}}_2$ clusters **3a** and **3b** emit phosphorescence sufficient for bioimaging in DMSO/PBS (1:1000, v:v) (Supplementary Figs. 73 and 74, Supplementary Table 30), we further examined their behavior in living cells to determine if there are differences in subcellular distribution and cell renewal pathway depending on the organic ligands.

Figure 5 shows the optimized bioimaging results for **3a**, **3b**, and **4**. At the concentration of 1.0 or 2.0 μM , where no cytotoxicity was observed by confocal microscopy analysis (Supplementary Figs. 75–82), **3a**, **3b**, and **4** entered HeLa cells within 10 min.

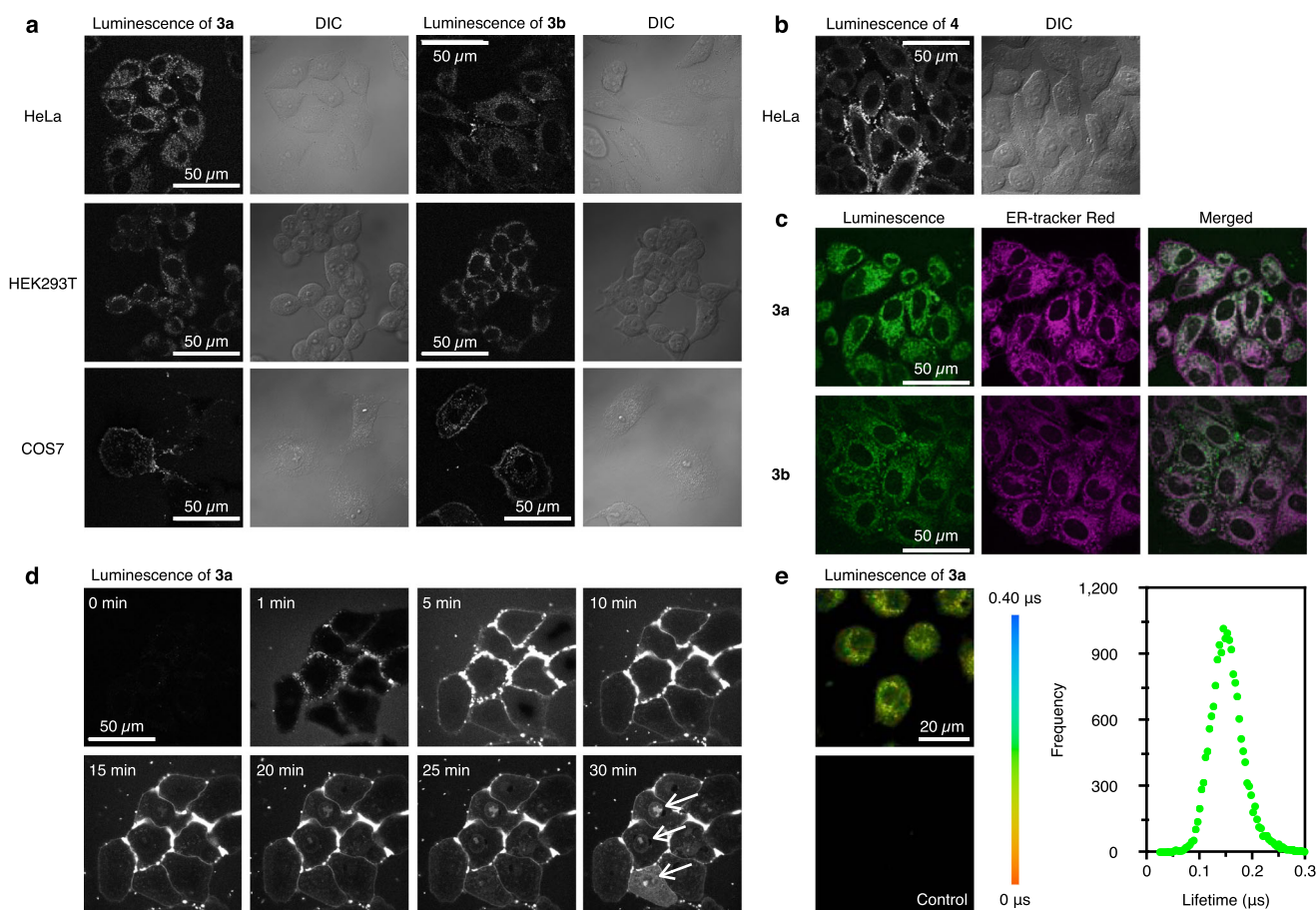


Fig. 5 Optimized bioimaging results of $\text{CAu}^{\text{I}}_6\text{Ag}^{\text{I}}_2$ clusters **3a**, **3b**, and **4**. **a** Confocal luminescence and differential interference contrast (DIC) images of **3a** and **3b** in HeLa, HEK293T, and COS7 cells. Scale bar, 50 μm . **b** Confocal luminescence and DIC images of **4** in HeLa cells. **c** Co-localization images of **3a** and **3b** with ER-tracker Red in HeLa cells. **d** Time-lapse images of **3a** in HeLa cells. White arrows indicate nuclear accumulation. **e** PLIM images and lifetime plot of **3a** in HeLa cells. Scale bar, 20 μm . Each experiment was independently repeated at least three times with similar results. As previously reported¹⁸, strong luminescence spots were observed in the nucleoli of the HeLa cells labeled with **4** at a concentration of 10 μM for 10 min. Time-lapse monitoring also confirmed that cellular uptake and nucleoli accumulation were fast under these conditions. At a concentration of 5.0 μM , similar localization was observed by extending the incubation time (30 and 60 min), but at the same time, the cells changed to a round shape and the nuclear envelope showed the characteristics of cells under stress⁴⁵. Similar nucleoli spots and morphological changes were also observed in the cells labeled with **3a-c** at a concentration of 5.0 or 10 μM . HEK293T cells and COS7 cells also showed a similar trend (Supplementary Figs. 75–81).

Clusters **3a** and **3b** were suggested to accumulate in specific organelles, whereas cluster **4** was uniformly distributed in the cytosol. HEK293T and COS7 cells labeled with **3a** or **3b** showed a similar distribution pattern. To identify the accumulated structures, the cells labeled with **3a** or **3b** were further labeled with several organelle markers. Confocal microscope analysis showed that **3a** and **3b** were selectively located in the ER. The time-lapse imaging revealed that clusters **3a** and **3b** were transported into the cells within 5 min after accumulation on the surface. **3a** or **3b** had accumulated in the ER after 10 min, and the longer the incubation time, the more it accumulated in the nucleus region (Fig. 5d and Supplementary Figs. 78, 80). The accumulation of **3a** in the ER, induced by a 10-min incubation, was maintained for 36 h (Supplementary Fig. 84). Thus, clusters with the NHC ligands can be selectively translocated to an intracellular organelle in a manner specific to the ligand structure. Furthermore, since these clusters have long emission lifetimes on the order of microseconds, phosphorescence lifetime imaging (PLIM) was conducted. The calculated lifetime of **3a** was 0.15 μs , which was in good agreement with the *in vitro* result. Thus, **3a** can be used as an ER-selective targeting reagent, and its phosphorescence can be well distinguishable from autofluorescence.

It is noteworthy that $\text{CAu}^{\text{I}}_6\text{Ag}^{\text{I}}_2$ clusters protected by the NHC or phosphine ligands showed different distributions in the cells, even though they have almost the same core structure. To clarify the cellular uptake pathway of **3a** and **4**, cells were incubated with **3a** and **4** at a lower temperature (4 $^{\circ}\text{C}$), where endocytosis was expected to be non-specifically inhibited. As shown in Fig. 6a, the cells labeled under the condition did not show any luminescence signals. Then, route-specific inhibitors such as wortmannin, sucrose, and genistein were used at 37 $^{\circ}\text{C}$ to specifically inhibit macropinocytosis, clathrin- and caveolin-dependent endocytosis, respectively. For cluster **3a** with benzimidazolylidene ligands, the genistein treatment effectively inhibited the ER accumulation. These results suggest that the uptake of cluster **3a** is due to a caveolin-dependent endocytosis process. In contrast, the accumulation of cluster **4** with phosphine ligands in the cytosol was blocked by all inhibitors. Thus cluster **4** was taken up into the cells and dispersed in a nonspecific manner. Based on these results, we proposed a possible route of cellular uptake and intracellular translocation of NHC- and phosphine-protected $\text{CAu}^{\text{I}}_6\text{Ag}^{\text{I}}_2$ clusters (Fig. 6b). These clusters first accumulate on the surface of the cell membrane and are then taken up into the cells by endocytosis.

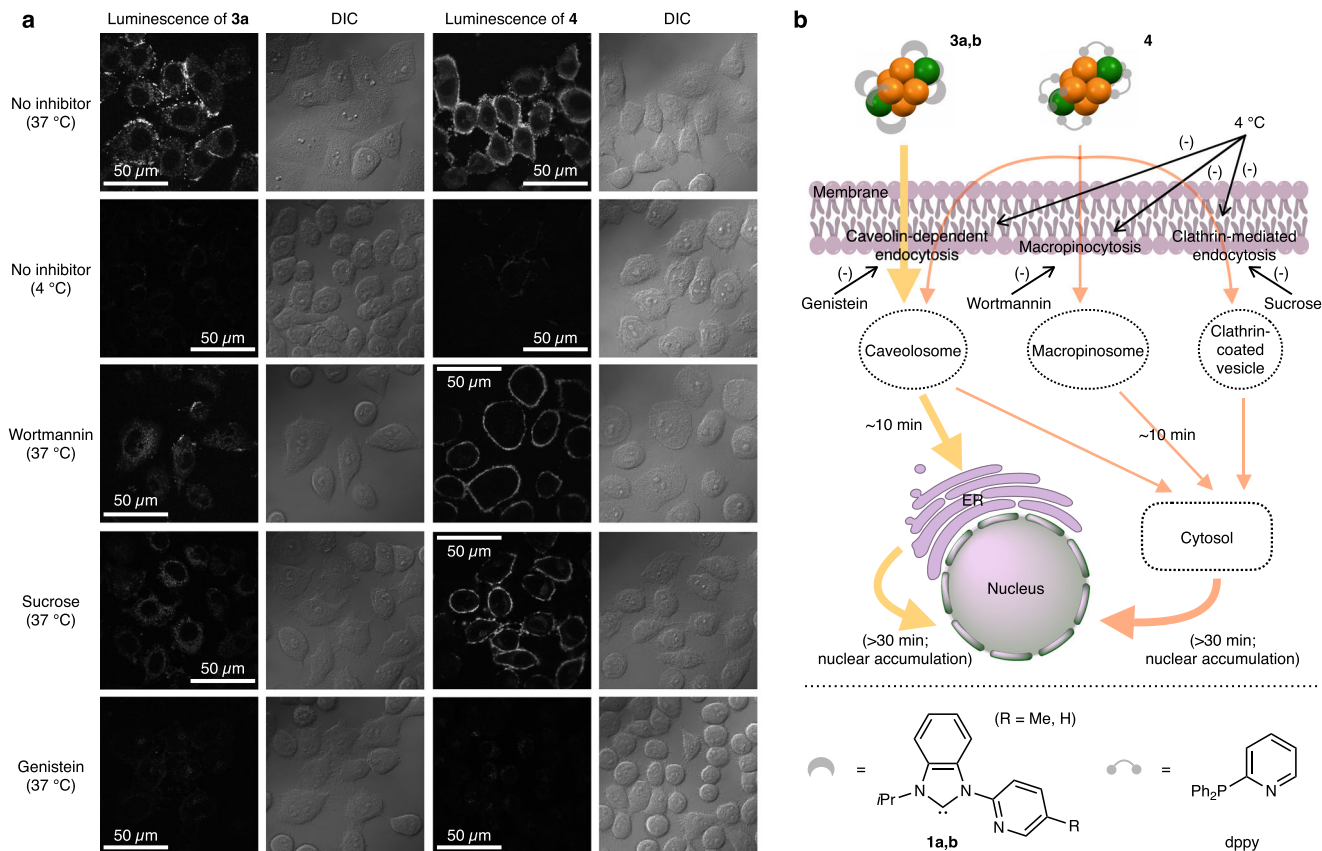


Fig. 6 Mechanisms and proposed routes of cellular uptake of carbene- and phosphine-protected $\text{CAu}_6\text{Ag}_{12}$ clusters. **a** Confocal luminescence and DIC images of clusters **3a** and **4** in HeLa cells at 37 °C without pretreatment of inhibitor (control), at 4 °C without pretreatment of inhibitor, or at 37 °C with pretreatment of endocytosis inhibitors wortmannin, sucrose or genistein. Scale bars, 50 μm . Each experiment was independently repeated at least three times with similar results. **b** Schematic representation of the proposed cellular uptake routes for carbene-protected **3a–d** and phosphine-protected **4**.

For phosphine-protected **4**, the uptake is an energy-dependent, nonspecific process that is associated with macropinocytosis, clathrin-mediated, and/or caveolin-dependent endocytosis. In the case of NHC-protected **3a–d**, caveolin-dependent endocytosis is the main pathway for cellular uptake. NHC-based clusters **3a** and **3b** were sequentially translocated to ER after intracellular uptake, but phosphine-based cluster **4** was released from intracellular compartments to cytosol within 10 min. Prolonged incubation allowed the nuclear accumulation of the clusters **3a**, **3b**, and **4**, which in turn increased the permeability of their membranes. In addition, high concentration of clusters accelerated these processes.

Discussion

In this study, we have established a rational design and synthesis method for a series of phosphorescent $\text{Au}^{\text{I}}\text{-Ag}^{\text{I}}$ clusters, and revealed that the organic ligands bound to the surface of the metal clusters are important for their photochemical property and subcellular distribution. The NHC ligands were found to remarkably shift the emission wavelength of the $\text{CAu}_6\text{Ag}_{12}$ clusters, and significantly affecting the phosphorescence quantum yield and lifetime, compared to the same cluster protected by phosphine ligands. More importantly, the $\text{CAu}_6\text{Ag}_{12}$ clusters were taken up into the living cells and showed structure-specific translocation pathways and distribution. This suggests that molecular design may be able to control molecular behaviors in the cell. Therefore, this study is expected to provide a strategy to create metal clusters with tunable functionalities, and also to lead to clear guidelines for designing active and applicable metallodrugs.

Methods

Synthesis of 1a-HI and 1b-HI. Under a nitrogen atmosphere, a Schlenk tube was charged with benzimidazole (5.00 g, 42.3 mmol), K_2CO_3 (3.90 g, 28.2 mmol), and the corresponding bromopyridine derivatives: 2-bromo-5-methylpyridine (2.43 g, 14.1 mmol) for **1a-HI** and 2-bromopyridine (1.37 mL, 14.1 mmol) for **1b-HI**. The reaction mixture was heated at 200 °C for 12 h and then allowed to cool to room temperature. After it was diluted with water (50 mL) and extracted with CH_2Cl_2 (50 mL \times 3), the combined organic phase was washed with sat. Na_2CO_3 aqueous solution (50 mL \times 3), and brine (50 mL), and then dried over anhydrous MgSO_4 before filtration. Concentration under reduced pressure gave a light red oil. This intermediate was then transferred into a Schlenk flask and dissolved in CH_3CN (50 mL) under a nitrogen atmosphere. 2-Iodopropane (1.51 mL, 15.2 mmol) was added to the solution, and the reaction mixture was heated at reflux for 12 h. After cooling to room temperature, the mixture was concentrated to ca. 5 mL under reduced pressure. When diethyl ether (50 mL) was added to this residue, a pale yellow precipitate was obtained as a crude product. Colorless crystals **1a-HI** and **1b-HI** were obtained by layering diethyl ether on $\text{CH}_2\text{Cl}_2/\text{CH}_3\text{CN}$ (9:1, v:v) solution containing the crude product. Yields: 2.30 g (43%, based on 2-bromo-5-methylpyridine) for **1a-HI**; 1.90 g (37%, based on 2-bromopyridine) for **1b-HI**.

For **1a-HI**: $^1\text{H NMR}$ (500 MHz, CDCl_3 , δ , ppm): 11.41 (s, 1H, benzimidazolyl), 8.77 (d, 1H, pyridyl), 8.61–8.59 (m, 1H, benzimidazolyl), 8.46 (d, 1H, pyridyl), 7.95 (dd, 1H, pyridyl), 7.84–7.82 (m, 1H, benzimidazolyl), 7.71 (td, 2H, benzimidazolyl), 5.39 (sept, 1H, isopropyl), 2.48 (s, 3H, methyl), 1.99 (d, 6H, isopropyl).

For **1b-HI**: $^1\text{H NMR}$ (500 MHz, CDCl_3 , δ , ppm): 11.46 (s, 1H, benzimidazolyl), 8.94 (d, 1H, pyridyl), 8.67 (m, 2H, benzimidazolyl + pyridyl), 8.16 (td, 1H, pyridyl), 7.86–7.84 (m, 1H, benzimidazolyl), 7.73 (t, 2H, benzimidazolyl), 7.54 (dd, 1H, pyridyl), 5.42 (sept, 1H, isopropyl), 2.01 (d, 6H, isopropyl).

Synthesis of 1c-HI. Under a nitrogen atmosphere, a Schlenk tube was charged with imidazole (2.04 g, 30.0 mmol), K_2CO_3 (2.76 g, 20.0 mmol), and 2-bromo-5-methylpyridine (1.72 g, 10.0 mmol). The reaction mixture was heated at 190 °C for 12 h and then allowed to cool to room temperature. After it was diluted with water (50 mL) and extracted with CHCl_3 (50 mL \times 3), the combined organic phases were washed with sat. Na_2CO_3 aqueous solution (50 mL \times 3), and then dried over anhydrous MgSO_4 before filtration. Concentration under reduced pressure gave a colorless oil, which was then transferred into a Schlenk flask and dissolved in

CH₃CN (50 mL) under a nitrogen atmosphere. 2-Iodopropane (1.70 g, 10.0 mmol) was added to the solution, and the reaction mixture was heated at reflux for 12 h. After cooling to room temperature, the mixture was concentrated to ca. 5 mL under reduced pressure. When diethyl ether (50 mL) was added to this residue, a pale yellow precipitate was obtained as a crude product. Colorless crystals of **1c-HI** were obtained by layering diethyl ether on CH₂Cl₂/CH₃CN (9:1, v:v) solution containing the crude product. Yield: 1.71 g (52%, based on 2-bromo-5-methylpyridine).

¹H NMR (500 MHz, CDCl₃, δ, ppm): 11.37 (s, 1H, imidazolyl), 8.54 (d, 1H, pyridyl), 8.32 (d, 1H, pyridyl), 8.26 (t, 1H, imidazolyl), 7.86 (dd, 1.8 Hz, 1H, pyridyl), 7.42 (t, 1H, imidazolyl), 5.27 (sept, 1H, isopropyl), 2.43 (s, 3H, methyl), 1.73 (d, 6H, isopropyl).

Synthesis of 2a–d. Imidazolium/benzimidazolium halide (**1a-HI** (114 mg, 0.30 mmol) for **2a**; **1b-HI** (110 mg, 0.30 mmol) for **2b**; **1c-HI** (98.7 mg, 0.30 mmol) for **2c**; **1d-HBr** (80.4 mg, 0.30 mmol) or **1d-HI** (94.5 mg, 0.30 mmol) for **2d**) was dissolved in dry CH₂Cl₂ (10 mL). Tht-AuCl (96.0 mg, 0.30 mmol) was added and then the solution was stirred for 5 min, which was followed by adding K₂CO₃ (828 mg, 6.00 mmol). After the mixture was stirred for 12 h in the dark, it was filtered through a thin layer of Celite. The solvent was then removed under reduced pressure using a rotary evaporator. After adding NaBF₄ (165 mg, 1.50 mmol) and CH₃OH (10 mL), the suspension was stirred for 5 min. CH₂Cl₂ (5 mL), a solution of KOH (28.0 mg, 0.50 mmol) in CH₃OH (3 mL), a solution of AgBF₄ (58.5 mg, 0.30 mmol) in CH₃OH (1 mL), and H₂O (50 μL) were sequentially dropwise added into the mixture under stirring, which leads to a brown suspension. After another 5 min stirring, the suspension was again filtered through Celite and evaporated to dryness. The solid was then transferred to a Schlenk flask with a nitrogen atmosphere, and dry CH₂Cl₂ (5 mL), Et₃N (30.0 μL, 0.20 mmol), and a 2.0 M solution of Me₃SiCHN₂ in hexanes (48.0 μL, 0.10 mmol) were added. The resulting mixture was stirred for another 1 h. After filtration into a tube, a layer of dry Et₂O was added to the CH₂Cl₂ solution, which gave the products colorless block-like crystals within 2 weeks. Yields: 59.5 mg (40%, based on tht-AuCl) for **2a**; 74.3 mg (52%, based on tht-AuCl) for **2b**; 31.3 mg (24%, based on tht-AuCl) for **2c**; 11.6 mg (9%, based on tht-AuCl (**1d-HBr**)) for **2d**; 10.0 mg (8%, based on tht-AuCl (**1d-HI**)) for **2d**.

For **2a**: ¹H NMR (500 MHz, CD₂Cl₂, δ, ppm): 8.40–8.15 (br, 6H, pyridyl), 7.91–7.38 (br, 30H, pyridyl + benzimidazolylidene), 7.22–6.72 (br, 6H, pyridyl), 5.75 (br, 6H, isopropyl), 1.45 (br, 54H, isopropyl + methyl). ¹³C NMR (126 MHz, CD₂Cl₂, δ, ppm): 187.9, 150.3, 148.5, 140.0, 135.6, 134.4, 132.4, 125.9, 125.7, 120.9, 113.8, 113.2, 54.3, 22.4, 18.3. ESI-MS (CH₂Cl₂): 1350.2 [(C)(Au-**1a**)₆]²⁺.

For **2b**: ¹H NMR (500 MHz, CD₂Cl₂, δ, ppm): 8.43 (s, 6H, pyridyl), 7.86 (br, 6H, pyridyl), 7.75 (m, 12H, benzimidazolylidene), 7.53 (m, 12H, benzimidazolylidene), 7.30 (br, 6H, pyridyl), 6.45 (br, 6H, pyridyl), 5.71 (br, 6H, isopropyl), 1.49 (br, 36H, isopropyl). ¹³C NMR (126 MHz, CD₂Cl₂, δ, ppm): 186.6, 151.0, 149.4, 139.1, 134.1, 132.2, 125.7, 125.7, 123.7, 121.3, 115.0, 113.3, 53.9, 21.9. ESI-MS (CH₂Cl₂): 1308.3 [(C)(Au-**1b**)₆]²⁺.

For **2c**: ¹H NMR (500 MHz, CD₂Cl₂, δ, ppm): 8.41 (d, 6H, pyridyl), 8.19 (s, 6H, pyridyl), 7.87 (s, 6H, imidazolylidene), 7.21 (s, 6H, imidazolylidene), 6.58 (d, 6H, pyridyl), 5.22 (sept, 6H, isopropyl), 2.08 (s, 18H, methyl), 1.15 (d, 36H, isopropyl). ¹³C NMR (126 MHz, CD₂Cl₂, δ, ppm): 179.8, 149.1, 148.7, 138.6, 133.9, 120.1, 117.2, 116.9, 53.6, 22.8, 18.1. ESI-MS (CH₂Cl₂): 1200.2 [(C)(Au-**1c**)₆]²⁺.

For **2d**: ¹H NMR (500 MHz, CD₂Cl₂, δ, ppm): 8.58 (d, 6H, pyridyl), 8.38 (d, 6H, pyridyl), 7.91 (s, 6H, imidazolylidene), 7.21 (s, 6H, imidazolylidene), 7.06 (dd, 6H, pyridyl), 6.85 (t, 6H, pyridyl), 5.20 (sept, 6H, isopropyl), 1.15 (d, 36H, isopropyl). ¹³C NMR (126 MHz, CD₂Cl₂, δ, ppm): 179.9, 150.9, 149.2, 138.2, 123.8, 120.3, 117.5, 117.5, 53.8, 23.0. ESI-MS (CH₂Cl₂): 1158.2 [(C)(Au-**1d**)₆]²⁺.

Synthesis of 3a–d. CAu^I cluster (**2a** (29.6 mg, 10.0 μmol) for **3a**; **2b** (28.8 mg, 10.0 μmol) for **3b**; **2c** (25.8 mg, 10.0 μmol) for **3c**; **2d** (24.9 mg, 10.0 μmol) for **3d**) was dissolved in dry CH₂Cl₂ (3 mL). AgBF₄ (6.0 mg, 30.0 μmol) in dry CH₃OH (1 mL) was added to the solution under stirring. The mixture was then filtered and the filtrate was layered with dry Et₂O. Yellow crystals can be obtained within 1 week. Yield: 30.3 mg (90%, based on **2a**) for **3a**; 30.2 mg (93%, based on **2b**) for **3b**; 26.3 mg (89%, based on **2c**) for **3c**; 18.3 mg (64%, based on **2d**) for **3d**.

For **3a**: ¹H NMR (500 MHz, CD₂Cl₂, δ, ppm): 7.91 (d, 6H), 7.81 (d, 6H), 7.74 (s, 6H), 7.64 (dt, 12H), 7.59 (t, 6H), 7.44 (d, 6H), 5.34 (sept, 6H, isopropyl), 1.41 (d, 18H, isopropyl), 1.34 (s, 18H, isopropyl), 1.12 (s, 18H, methyl). ¹³C NMR (126 MHz, CD₂Cl₂, δ, ppm): 183.6, 151.8, 147.4, 143.1, 137.2, 134.5, 131.9, 127.6, 127.1, 123.5, 114.1, 113.4, 54.1, 22.3, 22.1, 16.4. ESI-MS (CH₂Cl₂): 2389.2 [(C)(Au-**1a**)₄AgAg₂](BF₄)₂⁺.

For **3b**: ¹H NMR (500 MHz, CD₂Cl₂, δ, ppm): 8.14 (td, 6H), 7.84 (d, 6H), 7.77 (d, 6H), 7.71 (t, 6H), 7.64–7.61 (m, 12H), 7.37 (d, 6H), 7.37 (d, 6H), 6.30 (d, 6H), 5.28 (sept, 6H, isopropyl), 1.44 (d, 18H, isopropyl), 1.33 (d, 18H, isopropyl); ¹³C NMR (126 MHz, CD₂Cl₂, δ, ppm): 183.6, 151.6, 149.8, 143.2, 134.5, 131.9, 127.22, 127.16, 125.7, 124.7, 113.8, 112.9, 54.5, 22.6, 22.1. ESI-MS (CH₂Cl₂): 2897.5 [(C)(Au-**1b**)₆Ag](BF₄)₂⁺.

For **3c**: ¹H NMR (500 MHz, CD₂Cl₂/CD₃OD = 9:1 (v:v), δ, ppm): 7.91 (d, 6H), 7.67 (s, 6H), 7.57 (s, 6H), 7.51 (d, 6H), 7.38 (s, 6H), 4.72 (sept, 6H, isopropyl), 2.14

(s, 18H, methyl), 1.19 (d, 18H, isopropyl), 0.94 (d, 18H, isopropyl); ¹³C NMR (126 MHz, CD₂Cl₂, δ, ppm): 178.6, 150.8, 149.6, 143.1, 136.6, 123.0, 121.8, 119.7, 54.7, 23.0, 22.4, 18.8. ESI-MS (CH₂Cl₂): 2681.5 [(C)(Au-**1c**)₆Ag](BF₄)₂⁺.

For **3d**: ¹H NMR (500 MHz, CD₂Cl₂/CD₃OD = 3:1 (v:v), δ, ppm): 8.12 (t, 6H), 7.78 (d, 6H), 7.62 (d, 12H), 7.45 (d, 6H), 7.31 (t, 6H), 4.64 (sept, 6H, isopropyl), 1.16 (d, 18H, isopropyl), 0.96 (d, 18H, isopropyl). ESI-MS (CH₂Cl₂/CH₃OH = 9:1 (v:v)): 1939.2 [(C)(Au-**1d**)₄AuAg](BF₄)⁺.

X-ray crystallography. Intensity data of compounds **1a–c-HI**, **2a–d**, and **3a–d** were collected on a Rigaku XtaLAB Synergy-DW system (CuKα) at 93 K. The structures were solved by direct methods, and non-hydrogen atoms except for the disordered BF₄[−] and CH₂Cl₂ in **2b** were refined anisotropically by the least squares on F² using the SHELXTL program. The hydrogen atoms of organic ligands were generated geometrically; no attempt was made to locate the hydrogen atoms of disordered dichloromethane molecules in **2b** and water molecules in **2d**.

Reporting summary. Further information on research design is available in the Nature Research Reporting Summary linked to this article.

Data availability

The data that support the findings of this study are available within the manuscript and its supplementary information and from the corresponding author upon request. The X-ray crystallographic coordinates for structures reported in this article have been deposited at the Cambridge Crystallographic Data Centre (CCDC) under deposition numbers CCDC 2103969 (**1a-HI**), CCDC 2103970 (**1b-HI**), CCDC 2103971 (**1c-HI**), CCDC 2103972 (**2a**), CCDC 2103973 (**2b**), CCDC 2103974 (**2c**), CCDC 2103975 (**2d**), CCDC 2103976 (**3a**), CCDC 2103977 (**3b**), CCDC 2103978 (**3c**), and CCDC 2103979 (**3d**). These data can be obtained free of charge from the Cambridge Crystallographic Data Centre via http://www.ccdc.cam.ac.uk/data_request/cif.

Received: 27 November 2021; Accepted: 8 July 2022;

Published online: 10 August 2022

References

- Schmidbauer, H. & Schier, A. A briefing on aurophilicity. *Chem. Soc. Rev.* **37**, 1931–1951 (2008).
- Schmidbauer, H. & Schier, A. Aurophilic interactions as a subject of current research: an up-date. *Chem. Soc. Rev.* **41**, 370–412 (2012).
- Kang, X. & Zhu, M. Tailoring the photoluminescence of atomically precise nanoclusters. *Chem. Soc. Rev.* **48**, 2422–2457 (2019).
- Santiago-Gonzalez, B. et al. Permanent excimer superstructures by supramolecular networking of metal quantum clusters. *Science* **353**, 571–575 (2016).
- Huang, R.-W. et al. Hypersensitive dual-function luminescence switching of a silver chalcogenolate cluster-based metal-organic framework. *Nat. Chem.* **9**, 689–697 (2017).
- Lei, Z., Pei, X.-L., Jiang, Z.-G. & Wang, Q.-M. Cluster linker approach: preparation of a luminescent porous framework with NbO topology by linking silver ions with gold(I) clusters. *Angew. Chem. Int. Ed.* **53**, 12771–12775 (2014).
- Ryo, K. et al. Ultrabright luminescence from gold nanoclusters: rigidifying the Au(I)-thiolate shell. *J. Am. Chem. Soc.* **137**, 8244–8250 (2015).
- Li, Q. et al. A mono-cuboctahedral series of gold nanocluster: photoluminescence origin, large enhancement, wide tunability, and structure – property correlation. *J. Am. Chem. Soc.* **141**, 5314–5325 (2019).
- Weerawardene, K. L. D. M. et al. Luminescence and electron dynamics in atomically precise nanoclusters with eight superatomic electrons. *J. Am. Chem. Soc.* **141**, 18715–18726 (2019).
- Yao, C. et al. Giant emission enhancement of solid-state gold nanoclusters by surface engineering. *Angew. Chem. Int. Ed.* **59**, 8270–8276 (2020).
- Scherbaum, F., Grohmann, A., Huber, B., Krüger, C. & Schmidbauer, H. “Aurophilicity” as a consequence of relativistic effects: the hexakis(triphenylphosphaneaurio)methane dication [(Ph₃PAu)₆C]²⁺. *Angew. Chem. Int. Ed. Engl.* **27**, 1544–1546 (1988).
- Gabbai, F. P., Schier, A., Riede, J. & Schmidbauer, H. Synthesis of the hexakis(triphenylphosphane)gold(I) methanium (2+) cation from trimethylsilyldiazomethane; crystal structure determination of the tetrafluoroborate salt. *Chem. Ber.* **130**, 111–113 (1997).
- Lei, Z. & Wang, Q.-M. Homo and heterometallic gold(I) clusters with hypercoordinated carbon. *Coord. Chem. Rev.* **378**, 382–394 (2019).
- Jia, J.-H. & Wang, Q.-M. Intensely luminescent gold(I)-silver(I) cluster with hypercoordinated carbon. *J. Am. Chem. Soc.* **131**, 16634–16635 (2009).

- Yang, Y., Pei, X.-L. & Wang, Q.-M. Postclustering dynamic covalent modification for chirality control and chiral sensing. *J. Am. Chem. Soc.* **135**, 16184–16191 (2013).
- Jia, J.-H., Liang, J.-X., Lei, Z., Cao, Z.-X. & Wang, Q.-M. A luminescent gold(I)–copper(I) cluster with unprecedented carbon-centered trigonal prismatic hexagold. *Chem. Commun.* **47**, 4739–4741 (2011).
- Lei, Z., Pei, X.-L., Guan, Z.-J. & Wang, Q.-M. Full protection of intensely luminescent gold(I)–silver(I) cluster by phosphine ligands and inorganic anions. *Angew. Chem., Int. Ed.* **56**, 7117–7120 (2017).
- Chen, M. et al. A phosphorescent silver(I)–gold(I) cluster complex that specifically lights up the nucleolus of living cells with FLIM imaging. *Biomaterials* **34**, 4284–4295 (2013).
- Hopkinson, M. N., Richter, C., Schedler, M. & Glorius, F. An overview of N-heterocyclic carbenes. *Nature* **510**, 485–496 (2014).
- Smith, C. A. et al. N-heterocyclic carbenes in materials chemistry. *Chem. Rev.* **119**, 4986–5056 (2019).
- Zhukhovitskiy, A. V., MacLeod, M. J. & Johnson, J. A. Carbene ligands in surface chemistry: from stabilization of discrete elemental allotropes to modification of nanoscale and bulk substrates. *Chem. Rev.* **115**, 11503–11532 (2015).
- Zhong, R., Lindhorst, A. C., Groche, F. J. & Kühn, F. E. Immobilization of N-heterocyclic carbene compounds: a synthetic perspective. *Chem. Rev.* **117**, 1970–2058 (2017).
- Crudden, C. M. et al. Ultra stable self-assembled monolayers of N-heterocyclic carbenes on gold. *Nat. Chem.* **6**, 409–414 (2014).
- Wang, G. et al. Ballbot-type motion of N-heterocyclic carbenes on gold surfaces. *Nat. Chem.* **9**, 152–156 (2017).
- MacLeod, M. J. et al. Robust gold nanorods stabilized by bidentate N-heterocyclic-carbene–thiolate ligands. *Nat. Chem.* **11**, 57–63 (2019).
- Polgar, A. M., Weigend, F., Zhang, A., Stillman, M. J. & Corrigan, J. F. A N-heterocyclic carbene-stabilized coinage metal-chalcogenide framework with tunable optical properties. *J. Am. Chem. Soc.* **139**, 14045–14048 (2017).
- Jin, L. et al. Trinuclear gold clusters supported by cyclic (alkyl)(amino)carbene ligands: mimics for gold heterogeneous catalysts. *Angew. Chem., Int. Ed.* **53**, 9059–9063 (2014).
- Narouz, M. R. et al. N-heterocyclic carbene-functionalized magic-number gold nanoclusters. *Nat. Chem.* **11**, 419–425 (2019).
- Narouz, M. R. et al. Robust, highly luminescent Au₁₃ superatoms protected by N-heterocyclic carbenes. *J. Am. Chem. Soc.* **141**, 14997–15002 (2019).
- Shen, H. et al. Highly robust but surface-active: an N-heterocyclic carbene-stabilized Au₂₅ nanocluster. *Angew. Chem., Int. Ed.* **58**, 17731–17735 (2019).
- Ube, H., Zhang, Q. & Shionoya, M. A carbon-centered hexagold(I) cluster supported by N-heterocyclic carbene ligands. *Organometallics* **37**, 2007–2009 (2018).
- Lei, Z., Nagata, K., Ube, H. & Shionoya, M. Ligand effects on the photophysical properties of N,N'-diisopropylbenzimidazolylidene-protected C-centered hexagold(I) clusters. *J. Organomet. Chem.* **917**, 121271 (2020).
- Lei, Z., Pei, X.-L., Ube, H. & Shionoya, M. Reconstituting the C-centered hexagold(I) clusters with N-heterocyclic carbene ligands. *Bull. Chem. Soc. Jpn.* **94**, 1324–1330 (2021).
- Schmidbaur, H., Raubenheimer, H. G. & Dobrzańska, L. The gold–hydrogen bond, Au–H, and the hydrogen bond to gold, Au...H–X. *Chem. Soc. Rev.* **43**, 345–380 (2014).
- Rigoulet, M. et al. Evidence for genuine hydrogen bonding in gold(I) complexes. *Proc. Natl Acad. Sci. USA* **116**, 46–51 (2019).
- Bakar, M. A., Sugiuchi, M., Iwasaki, M., Shichibu, Y. & Konishi, K. Hydrogen bonds to Au atoms in coordinated gold clusters. *Nat. Commun.* **8**, 576 (2017).
- Greisch, J.-F. et al. Gas-phase photoluminescence and photodissociation of silver-capped hexagold clusters. *J. Phys. Chem. A* **122**, 5799–5810 (2018).
- Aikens, C. M. Electronic and geometric structure, optical properties, and excited state behavior in atomically precise thiolate-stabilized noble metal nanoclusters. *Acc. Chem. Res.* **51**, 3065–3073 (2018).
- Weerawardene, K. L. D. M. & Aikens, C. M. Theoretical insights into the origin of photoluminescence of Au₂₅(SR)₁₈[–] nanoparticles. *J. Am. Chem. Soc.* **138**, 11202–11210 (2016).
- Wang, F. & Ziegler, T. A simplified relativistic time-dependent density-functional theory formalism for the calculations of excitation energies including spin-orbit coupling effect. *J. Chem. Phys.* **123**, 154102 (2005).
- Te Velde, G. et al. Chemistry with ADF. *J. Comput. Chem.* **22**, 931–967 (2001).
- Zhou, M., Lei, Z., Guo, Q., Wang, Q.-M. & Xia, A. Solvent dependent excited state behaviors of luminescent gold(I)–silver(I) cluster with hypercoordinated carbon. *J. Phys. Chem. C* **119**, 14980–14988 (2015).
- Harvey, J. N. & Aschi, M. Spin-forbidden dehydrogenation of methoxy cation: a statistical view. *Phys. Chem. Chem. Phys.* **1**, 5555–5563 (1999).
- Harvey, J. N., Aschi, M., Schwarz, H. & Koch, W. The singlet and triplet states of phenyl cation. A hybrid approach for locating minimum energy crossing points between non-interacting potential energy surfaces. *Theor. Chem. Acc.* **99**, 95–99 (1998).
- New, E. J., Parker, D., Smith, D. G. & Walton, J. W. Development of responsive lanthanide probes for cellular applications. *Curr. Opin. Chem. Biol.* **14**, 238–246 (2010).
- Zhao, Q., Huang, C. & Li, F. Phosphorescent heavy-metal complexes for bioimaging. *Chem. Soc. Rev.* **40**, 2508–2524 (2011).
- Lo, K. K.-W. Molecular design of bioorthogonal probes and imaging reagents derived from photofunctional transition metal complexes. *Acc. Chem. Res.* **53**, 32–44 (2020).

Acknowledgements

This research was supported by JSPS KAKENHI Grants No. JP16H06509 (Coordination Asymmetry) and No. JP21H00453 to M.S., JSPS KAKENHI Grant No. JP19K05538 to M.E., and CREST (JPMJCR1752) from Japan Science and Technology (JST) to T.O. Part of the computation was performed using Research Center for Computational Science, Okazaki, Japan (Project: 20-IMS-C100).

Author contributions

Z.L. designed this work, performed synthetic experiments, analyzed data, and prepared the manuscript. M.Endo performed bioimaging experiments, analyzed data, and prepared the manuscript. H.U. designed this work and directed the research. T.S., P.Z., K.N., and M.Ehara performed theoretical calculations. X.-L.P. assisted in the synthetic experiments. T.E. performed PLIM experiments. T.K., and T.O. directed experiments. M.S. proposed and supervised this study and prepared the manuscript.

Competing interests

The authors declare no competing interests.

Additional information

Supplementary information The online version contains supplementary material available at <https://doi.org/10.1038/s41467-022-31891-3>.

Correspondence and requests for materials should be addressed to Masahiro Ehara, Takeaki Ozawa or Mitsuhiko Shionoya.

Peer review information *Nature Communications* thanks Hannu Häkkinen and other anonymous reviewer(s) for their contribution to the peer review of this work.

Reprints and permission information is available at <http://www.nature.com/reprints>

Publisher's note Springer Nature remains neutral with regard to jurisdictional claims in published maps and institutional affiliations.



Open Access This article is licensed under a Creative Commons Attribution 4.0 International License, which permits use, sharing, adaptation, distribution and reproduction in any medium or format, as long as you give appropriate credit to the original author(s) and the source, provide a link to the Creative Commons license, and indicate if changes were made. The images or other third party material in this article are included in the article's Creative Commons license, unless indicated otherwise in a credit line to the material. If material is not included in the article's Creative Commons license and your intended use is not permitted by statutory regulation or exceeds the permitted use, you will need to obtain permission directly from the copyright holder. To view a copy of this license, visit <http://creativecommons.org/licenses/by/4.0/>.

© The Author(s) 2022